Resolving Runaway Electron Distributions in Space, Time, and Energy

C. Paz-Soldan,[1] C. M. Cooper,[2] P. Aleynikov,[3] N. W. Eidietis,[1] A. Lvovskiy,[2] D. C. Pace,[1] D. P. Brennan,[4] E. M. Hollmann,[5] C. Liu,[4] R. A. Moyer,[5] and D. Shiraki[6]

[1] *General Atomics, San Diego, CA, USA**
[2] *Oak Ridge Associated Universities, Oak Ridge, TN, USA*
[3] *Max-Planck Institute for Plasma Physics, Greifswald, Germany*
[4] *Princeton University, Princeton, NJ, USA*
[5] *University of California San Diego, La Jolla, CA, USA*
[6] *Oak Ridge National Laboratory, Oak Ridge, TN, USA*

(Dated: January 30, 2018)

Areas of agreement and disagreement with present-day models of RE evolution are revealed by measuring MeV-level bremsstrahlung radiation from runaway electrons (REs) with a pinhole camera. Spatially-resolved measurements localize the RE beam, reveal energy-dependent RE transport, and can be used to perform full two-dimensional (energy and pitch-angle) inversions of the RE phase-space distribution. Energy-resolved measurements find qualitative agreement with modeling on the role of collisional and synchrotron damping in modifying the RE distribution shape. Measurements are consistent with predictions of phase-space attractors that accumulate REs, with non-monotonic features observed in the distribution. Temporally-resolved measurements find qualitative agreement with modeling on the impact of collisional and synchrotron damping in varying the RE growth and decay rate. Anomalous RE loss is observed and found to be largest at low energy. Possible roles for kinetic instability or spatial transport to resolve these anomalies are discussed.

I. INTRODUCTION

Due to the severe potential for damage to the reactor walls, runaway electrons (REs) pose a significant operational risk to fusion-grade tokamaks such as ITER [1–4]. RE populations are accelerated to very high energy (tens of MeV) by the large electric fields induced during a tokamak disruption. The first line of defense against REs is to avoid their generation by either avoiding disruptions entirely, or by developing disruption mitigation strategies that prevent the formation of runaway electrons. A second line of defense is to manipulate the post-disruption RE beam to dissipate its energy prior to contact of the RE beam with the material surface. An example action is the injection of a large quantity of high-Z nobel gas, either in frozen or gaseous form.

Empirical tuning of RE control actuators in future tokamaks will be limited due to the potential for damage. Instead, a predictive understanding is needed to select and optimize actuators for RE control. Present-day experiments have a crucial role to play in validating theoretical predictions of RE dissipation. This role is most direct in the second line of defense, where similar conditions to what is expected in ITER can be accessed in existing tokamaks.

Theory and modeling work to understand the dissipation of RE populations is actively pursued. Early models taking into account small angle Coulomb collisions [5] and later large angle collisions [6] identified the crucial role of the 'critical electric field' (E_C), which defines the electric field at which collisional drag balances electric field acceleration in the relativistic limit. Later work identified the potential for synchrotron damping to elevate the effective E_C [7, 8], and more recently analytic treatments[9] and computational methods [10–16] were developed to combine the effects of synchrotron damping and pitch-angle scattering off high-Z ions. These works confirmed that synchrotron and pitch-angle scattering can together elevate the effective E_C above early model predictions.

Several experiments concurrently yielded evidence of very elevated E_C values above both the early model prediction and the elevated E_C from more modern models [17–19], both using trace-level REs naturally occurring in low density Ohmic plasmas as well as in post-disruption 'plateau' RE beams [20, 21]. More recently, diagnostic improvements enabled new experimental resolution in both space and time to measure the RE distribution function, yielding improved comparison to modeling [22]. This work found that while most qualitative trends were captured, quantitative discrepancies remained. Most notably, theory did not yet match the experimentally observed very elevated E_C.

In this paper precise measurements of RE distribution functions and dissipation rates in the spatial, temporal, and energy domains are presented, enabled by a new RE diagnostic called the 'Gamma Ray Imager' (GRI) [23, 24] deployed on the DIII-D tokamak. Direct comparisons to modeling are made wherever possible, highlighting areas of agreement and disagreement. This paper expands on measurements first presented in Ref. 22 by 1) describing experimental methodology and model comparisons in greater detail, 2) describing expected spatial effects using a synthetic diagnostic, 3) presenting supporting measurements from additional diagnostics, 4) and discussing candidate mechanisms to explain the observed discrepancies.

* paz-soldan@fusion.gat.com

The remainder of this paper is structured as follows. Section II describes the measurement technique and plasma scenario employed in this work. Section III describes measurements in the spatial domain and how radial and angular RE profiles are resolved. Section IV describes the inversion of RE energy distributions from localized hard X-ray (HXR) emission and subsequent comparison of RE distribution shapes against theoretical predictions as dissipation terms are varied. Section V describes time-domain measurements of RE emission growth and decay, including parametric dependencies and comparisons to theoretical predictions. Finally, a summary of observations along with areas for further improvements in modeling and measurement are provided in Sec. VI.

II. DESCRIPTION OF DIAGNOSTIC, PLASMA SCENARIO, AND MODELING APPROACH

A. Diagnostic Sensitivity

This work focuses on measurements of the RE population made by the GRI system installed on DIII-D [23, 24]. The GRI is a tangentially-viewing pinhole camera made of lead, with collimation provided along 123 discrete sight-lines as shown in Fig. 1(a). When a RE scatters off a plasma nuclei, HXR emission is generated via the bremsstrahlung mechanism. If the HXR is emitted along a sight-line of the GRI, the HXR will enter the pinhole and be registered on a pulse-height counting detector consisting of an integrated Bismuth-Germanate (BGO) scintillating crystal, a photo-diode, and pre-amplification electronics. The output of each detector is digitized at 10 MHz sample rate, enabling individual pulses to be discriminated, as shown in Fig. 1(b). The height of the pulse corresponds linearly to the energy of the measured HXR (E_γ). Each HXR pulse is assigned an energy and a time-stamp, and histograms are later formed to build up time-resolved distributions of the RE HXR emission (f_γ) along each sight-line. As will be described in Sec. IV, the HXR energy distribution (f_γ) in turn carries information about the incident RE distribution (f_e), which can be inverted with some assumptions. Each sight-line views a different part of the plasma cross-section, as shown in Fig. 1(c). Along each sight-line, different angles are made between the equilibrium magnetic field direction ($\hat{b}$, obtained from equilibrium reconstructions) and the sight-line orientation ($\hat{k}$). The minimum $\theta_{\hat{k}\hat{b}}$ along the sight-line is used to color-code the view. The $\theta_{\hat{k}\hat{b}}$ parameter is crucial to understand the spatial dependence of the emission, as will be described in Sec. III. Note that of the 123 available sight-lines, approximately 20 were populated for these first experiments. Further details of the diagnostic are provided in Refs. 23 and 24.

Beyond the GRI, measurements of the RE population are also made with diagnostics sensitive to bremsstrahlung and synchrotron radiation from distinct parts of RE phase space, as summarized in Fig. 2. DIII-D is equipped with several scintillating HXR detectors placed several meters from the tokamak, here called the 'distant HXR' detectors. These detectors have no collimation and thus sample the entire distribution with uncertain weighting. This sort of diagnostic was previously used to identify elevated thresholds for the transition from RE growth to decay [18, 19]. Synchrotron emission (SE) is measured in the visible range by a tangentially viewing camera system, capable of generating detailed spatial images of the RE emission intensity pattern. These images have been reported in several experimental publications [25–27] and only recently has the SE shape been predicted by simulation [28, 29]. Sensitivity scans in simulation indicate that the visible SE originates from quite energetic REs of medium pitch-angle. Finally, electron cyclotron emission (ECE) radiometers at high frequency (here from 140-300 GHz) are preferentially sensitive to non-thermal synchrotron emission from REs. Due to the radial viewing geometry of the ECE radiometers on DIII-D, these diagnostics probe the high pitch-angle RE population. Simulation further indicates that for these frequencies the energy of the RE responsible for the emission is low [15]. While this work focuses on the GRI system, measurements from these other diagnostics are also presented to corroborate GRI observations.

B. Scenario Description

This work reports measurements made in low density Ohmic plasmas during flat-top. Low density operation free from error field penetration supports the excitation of trace-level RE populations through the 'Dreicer' mechanism [30], which as time goes on begin to multiply through the secondary ('Avalanche') mechanism. A typical discharge evolution is shown in Fig. 3, with the early period with strong primary and secondary generation termed the growth phase. Typical parameters in the growth phase are electron density (n_e) of 0.5×10^{19} m^{-3}, electron temperature (T_e) of 1.8 keV, toroidal field (B_T) of 1.4 T, plasma current (I_P) of 0.8 MA, and loop voltage (V_{loop}) of 0.6 V.[18] A typical avalanche multiplication time in these conditions is 0.5 s, thus several multiplications occur during the growth phase. During this time the distant HXR signal increases several-fold exponentially [Fig. 3(b)].

After several seconds the discharge transitions to the 'dissipation phase', where plasma parameters are changed to observe their effect on the RE distribution. As the dissipation phase usually involves gas puffing to raise n_e, the transition time is denoted t_{puff}. While previously t_{puff} occurred at a fixed time, the DIII-D plasma control system was upgraded to allow asynchronous control based on the magnitude of high-harmonic ECE at 140 GHz, a frequency where the ECE is dominated by non-thermal emission. As seen in Fig. 3(c), when the

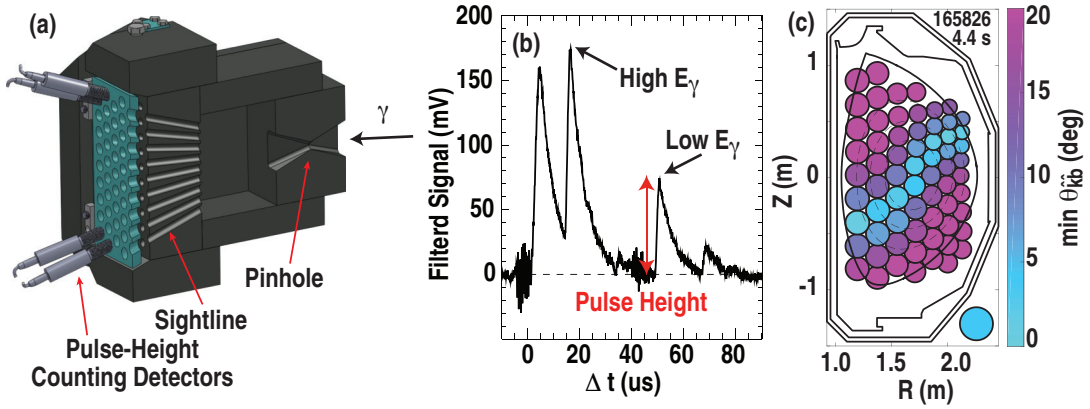

FIG. 1. (a) GRI pinhole camera geometry, (b) raw digitized signal from a single detector, and (c) sight-lines into the plasma at the tangency plane. Colors indicate the minimum angle ($\theta_{\hat{k}\hat{b}}$) between the magnetic field orientation ($\hat{b}$) and the sight-line orientation ($\hat{k}$).

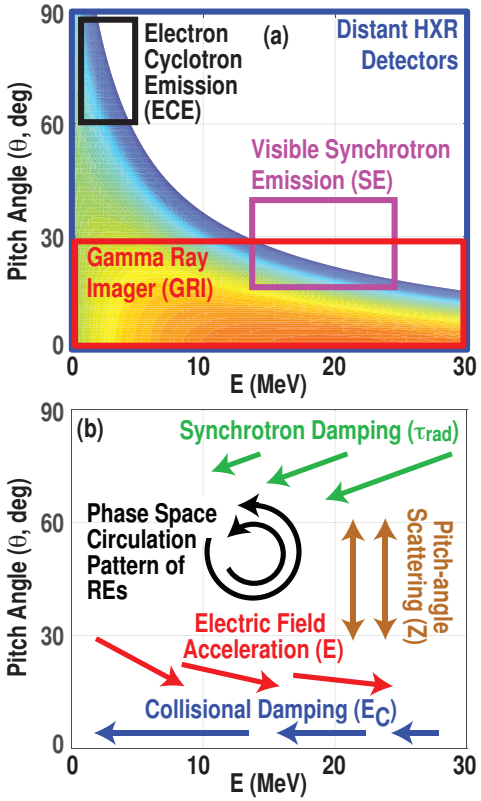

FIG. 2. (a) Region of phase space responsible for emission measured by the various diagnostics used in these experiments, together with an example predicted f_e (color contours) to indicate where REs are expected in phase space. (b) Cartoon description of influence of electric field acceleration, collisional damping, pitch-angle scattering, and synchrotron damping on REs in phase space.

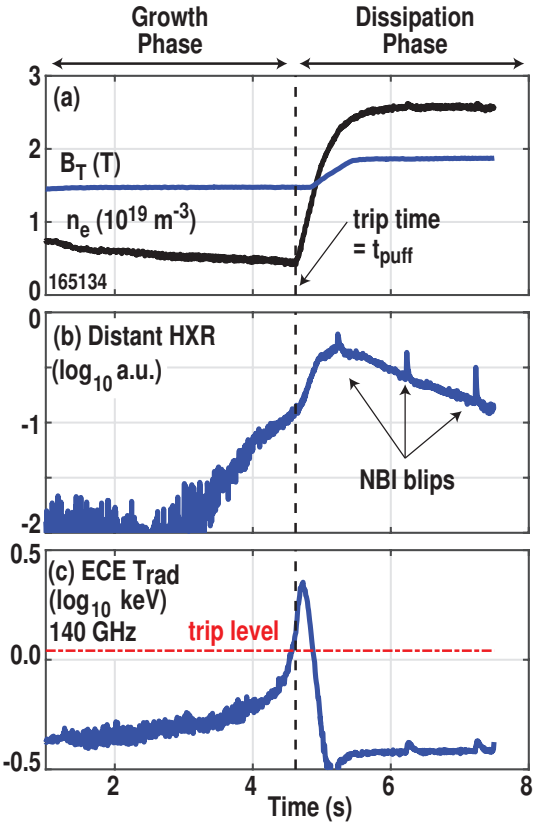

FIG. 3. Evolution of (a) n_e and B_T, (b) distant HXR detector, and (c) ECE radiometer illustrating the asynchronous transition from a RE growth to RE dissipation phase when a critical level of ECE emission is reached. Experiments discussed herein are conducted by varying the plasma parameters in only the dissipation phase.

ECE emission exceeds a pre-set trip level the dissipation phase is entered. Maintaining a constant trip level enables roughly the same RE distribution to be achieved in every pulse prior to entering the dissipation phase. If the trip is not enabled, the rapid rise in ECE progresses and the discharge evolves to tearing instability as described in Ref. 31.

C. Modeling Approach

In order to predict expected RE distribution functions (f_e) and growth or decay rates, the time-evolution of non-dimensional parameters determining the RE distribution must be known. In contrast to the complex and rapid dynamics of a disruptive plasma, both the growth and

decay phase of the Ohmic plasma are quasi-stationary and all relevant parameters are measured with sufficient time-resolution. This generates uniquely confident input parameters to modeling. The modeling inputs include the ratio of the imposed electric field E to the critical electric field $E_{\rm C}$, defined as

$$\frac{E}{E_{\rm C}} \equiv \frac{4\pi\varepsilon_0^2 m_e V_C^2}{n_e e^3 \ln\Lambda} \approx 10\frac{V_{\rm loop}[{\rm V}]}{n_e[10^{19}{\rm m}^{-3}]}, \qquad (1)$$

and the ratio of the collision time to the synchrotron damping time $\hat{\tau}_{\rm rad}$, defined as

$$\hat{\tau}_{\rm rad} \equiv \frac{3}{2}\left(\frac{m_e \ln\Lambda}{\epsilon_0}\right)\frac{n_{\rm e}}{B_T^2} \approx 28\frac{n_e[10^{19}{\rm m}^{-3}]}{(B_T[{\rm T}])^2}. \qquad (2)$$

In addition, the effective charge Z, important for pitch-angle scattering, is controlled by deliberate injection of a nitrogen impurity species and is measured using charge-exchange spectroscopy of both nitrogen and ambient carbon populations. Finally, the electron temperature T_e, important for Dreicer generation, is measured with Thomson scattering. The impact of these different effects (electric field acceleration, collisional damping, pitch-angle scattering, and synchrotron damping) in RE phase space is shown in cartoon format in Fig 2(b). With all effects acting together, circulation patterns in RE phase space can be formed.

To model the evolution of f_e the time-dependent relativistic 2-D Fokker-Planck equation (such as Ref. [32]) is solved numerically inputting measured on-axis (spatially 0-D) plasma parameters of $E/E_{\rm C}$, $\hat{\tau}_{\rm rad}$, and Z. The equation as in Ref. [9] is solved with two amendments. First, the collision operator is extended to be valid for lower energies using an approach similar to Refs. [33, 34]. Second, an approximate secondary source is included which captures the effect of a finite energy incident electron population. This treatment accurately captures the analytical results of RE generation models [5, 6, 35] as well as the near-threshold regime [9]. This process generates a complete two-dimensional f_e, which is then integrated from pitch-angle of 0 to 30°, corresponding to the approximate angular coverage of the GRI system as will be described in Sec. III.

D. Relevance to ITER Post-Disruption Conditions

Owing to the wide variety of plasma parameters ($n_e, B_T, V_{\rm loop}$) accessible in the dissipation phase, non-dimensional parameters $E/E_{\rm C}$, $\hat{\tau}_{\rm rad}$, and Z can be made surprisingly similar to those expected in ITER post-disruptive conditions. For example, owing to the low B_T of these plasmas (1.4 T) as compared to ITER (5.3 T), to match the expected value of $\hat{\tau}_{\rm rad}$ (≈ 70) during a post-disruption ITER RE beam requires very low density operation in DIII-D. In terms of Z, impurity injection in the Ohmic plasmas has raised Z to about 4, similar to the expectation of $Z \approx 5$ in ITER for partially-assimilated neon secondary injection. A wide range of $E/E_{\rm C}$ is expected during a single discharge in ITER, ranging from 1–2 to several hundred [36, 37], whereas in these plasmas $E/E_{\rm C}$ is well controlled between $\approx$ 2–8. It should be noted significant uncertainty exists in the parameters expected for ITER, largely owing to uncertainties in the degree of impurity assimilation. Thus, these experiments are not meant to match any specific prediction for ITER, but rather explore effects in a parametric space that should overlap with eventual ITER values.

Notwithstanding the surprisingly good non-dimensional match of ($E/E_{\rm C}$,$\hat{\tau}_{\rm rad}$, and Z) to expected ITER conditions, the low density scenario is not expected to yield ITER-relevant results for some aspects of the RE problem. For example, as these plasmas are fully ionized, they cannot be used to validate predictions of enhanced dissipation due to partial screening [38, 39], nor would they be well suited to understand phenomenology associated with the RE final loss [40]. Impurity transport into a low density Ohmic plasma with REs is also likely not a valid analog to the post-disruption condition [41].

III. RESOLVING THE SPATIAL DOMAIN: RADIAL AND PITCH-ANGLE RE PROFILES

Each collimated sight-line of the GRI system views a different portion of the plasma cross section, as shown in Fig. 1(c). By comparing the emission recorded along each sight-line, information about the spatial and angular distribution of the RE population can be inferred. However, in order to interpret these measurements the expected diagnostic sensitivity to spatially uniform and mono-energetic RE populations must first be understood. The expected sensitivity is computed using the synthetic diagnostic introduced in Sec. II A, with a complete description given in Ref. 24. This section will explore synthetic diagnostic dependencies alongside a comparison to experimental data.

The synthetic diagnostic is used to predict the HXR emission shape from a uniform RE density ($n_{\rm RE}$) beam of a certain minor radius $r_{\rm beam}$. This beam is given a single electron energy (E_e), and zero pitch-angle. The expected emission as a function of E_γ is then computed for all of the sight-lines that intersect the plasma. As shown in Fig. 4, $r_{\rm beam}$ increases the size of the emission spot, while increasing E_e increases the sharpness along the line of low $\theta_{\hat{k}\hat{b}}$.

This study identifies two directions most useful for reduced analysis. First, for analysis of the radial profile, it is useful to focus on the line of low $\theta_{\hat{k}\hat{b}}$ as this de-emphasizes changes due to E_e variations. Second, for analysis of the phase space profile, important information can be gained by comparing emission from different sight-lines sampling the same flux surface. These direc-

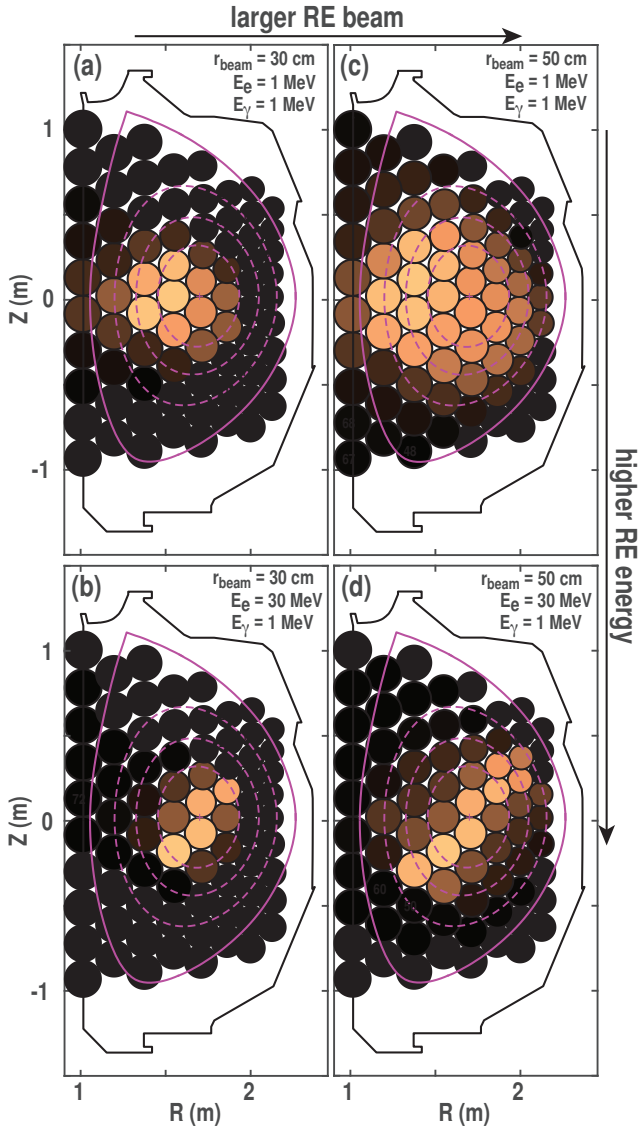

FIG. 4. Synthetic diagnostic prediction of HXR emission intensity pattern at a single E_γ as a function of $r_{\rm beam}$ and E_e, assuming zero pitch-angle. Increasing $r_{\rm beam}$ increases the size of the emission spot, while increasing E_e increases the sharpness along the line of low $\theta_{\hat{k}\hat{b}}$.

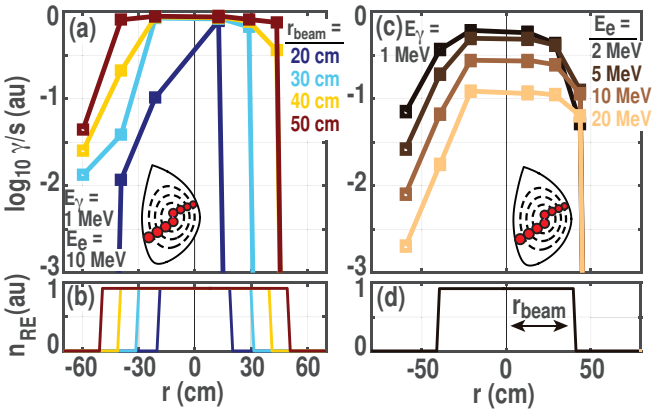

FIG. 5. Synthetic diagnostic predictions of the dependence of emission along the low $\theta_{\hat{k}\hat{b}}$ line to (a-b) $r_{\rm beam}$ and (c-d) E_e. The inset indicates the sight-lines considered.

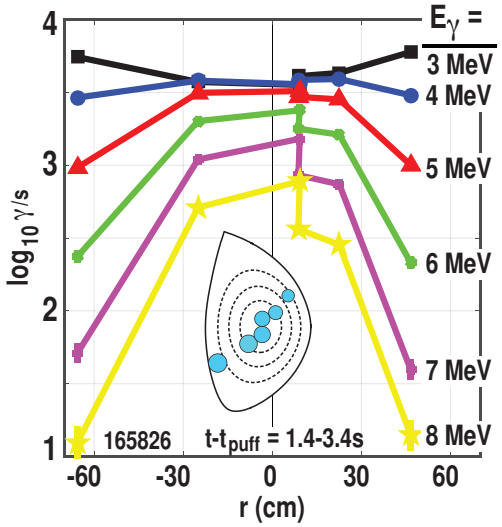

FIG. 6. Experimental measurement of the emission dependence along the low $\theta_{\hat{k}\hat{b}}$ line as a function of E_γ, indicating a convolution of the $r_{\rm beam}$ and E_e effects isolated in Fig. 5.

tions will now be considered separately in Sections III A and III B.

Note that the bremsstrahlung rate coefficients indicate that while the shape of the emission is very sensitive to E_e, there is no significant spatial variation with E_γ for constant E_e. Thus, for all model-produced images $E_\gamma = 1$ MeV is used. Note also that the synthetic diagnostic at present uses a zero-pitch angle approximation, which future work will relax.

A. Radial Profile Resolution

Synthetic diagnostic predictions along the low $\theta_{\hat{k}\hat{b}}$ line are examined as a function of E_e and $r_{\rm beam}$. As seen in Fig. 4, a strong sensitivity of the emission along the low $\theta_{\hat{k}\hat{b}}$ line is expected with $r_{\rm beam}$. Focusing on the low $\theta_{\hat{k}\hat{b}}$ line, the dominant effect of $r_{\rm beam}$ is seen in Fig. 5(a). Larger and smaller $r_{\rm beam}$ map directly onto larger and smaller emission patterns. The break in the emission is especially sharp along the low-field side (LFS), while on the high-field side (HFS) it is more gradual. That the emission is asymmetric from LFS to HFS is reminiscent of the synchrotron emission images [ex. Fig. 12(f)].

The effect of E_e along the low $\theta_{\hat{k}\hat{b}}$ line is more muted, as can be seen in Fig. 5(c). As E_e is increased, a larger decrease is found on the HFS than on the LFS. This supports the interpretation that the increased signal on the HFS is simply an instrumental effect resulting from the longer integration lengths along inboard sight-lines, since at higher E_e the emission is more localized to the tangency plane as opposed to coming from the entire sight-line [24]. Further LFS/HFS asymmetries may arise from untreated finite pitch-angle effects.

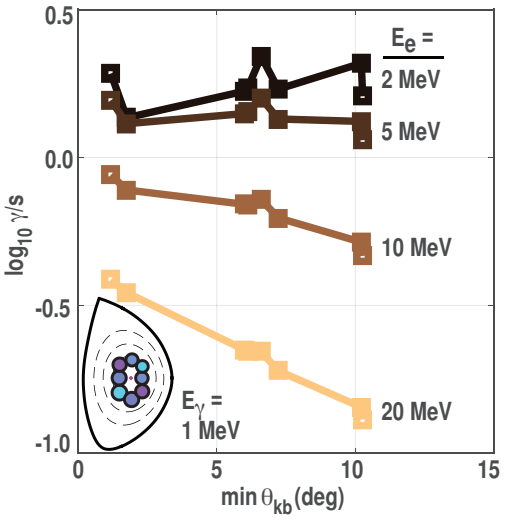

FIG. 7. Synthetic diagnostic prediction of emission variations between sight-lines viewing the same flux surface as E_e is varied with fixed n_{RE} and r_{beam}, illustrating increased sharpness to low $\theta_{\hat{k}\hat{b}}$ at high E_e. Data is plotted against the minimum $\theta_{\hat{k}\hat{b}}$ of the sight-line.

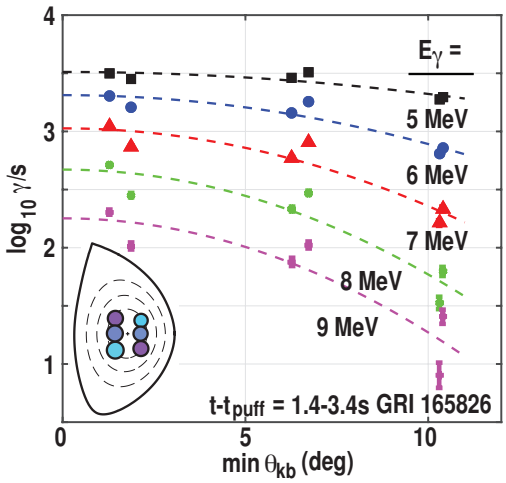

FIG. 8. Experimentally measured emission along the same sight-lines, with significantly more emission measured at low $\theta_{\hat{k}\hat{b}}$.

Since the RE current is predominantly carried by few-MeV electrons [3], these measurements can be used to measure the size of the RE current channel. This is an advantage over conventional visible SE images, since these images are dominated by the few highest energy electrons ($\geq$ 15 MeV [28, 29]) and the current carried by these electrons is vanishingly small.

Experimental measurements along the low $\theta_{\hat{k}\hat{b}}$ line, shown in Fig. 6 indicate a strong variation of the RE beam size with E_γ and thus E_e, and appear to have a convolution of the E_e and r_{beam} effects isolated in Fig. 5. This indicates that energy-dependent transport mechanisms are acting, although their origin is not yet understood. Measurements are also consistent with an asymmetry from LFS to HFS.

These radial measurements constitute a new frontier for RE model validation, as the vast majority of existing models do not include spatial effects, sacrificing spatial degrees of freedom to focus on phase space effects. Where spatial variations are treated, it is usually with an ad-hoc diffusion coefficient for the RE population [42]. These measurements can serve to empirically measure diffusion coefficients and understand their parametric dependencies.

B. Angular Profile Resolution

Synthetic diagnostic dependencies along a given flux surface are found to be most strongly sensitive to E_e, shown in Fig. 7 and better representing the increased 'sharpness' of the emission pattern in Fig. 4. The simplification of zero pitch-angle used, however, has direct implications for this spatial direction. This is because in the limit of high E_e, forward beamed emission would still reach a sight-line with high $\theta_{\hat{k}\hat{b}}$ if the electron pitch-angle matches $\theta_{\hat{k}\hat{b}}$. Thus, emission profiles along the same flux surface contain information on the pitch-angle distribution of the RE population, which future work will examine.

The importance of pitch-angle can be seen by considering experimental measurements along these same slight-lines, shown in Fig. 8. Significant variations are seen with E_γ from 5–9 MeV. This is greater than the variation expected from increasing E_e from 5 to 9 MeV at constant n_{RE} (shown in Fig. 7)), and thus indicates the underlying n_{RE} is varying with E_e. Further, the increased localization to low $\theta_{\hat{k}\hat{b}}$ of the $E_\gamma = 9$ MeV emission indicates some of this emission is be due to electrons with $E_e > 9$ MeV. These measurements point to the future possibility of full two-dimensional inversions of the RE distribution function, with energy information provided by f_γ and angular information provided by comparison of views of the same flux surface and different $\theta_{\hat{k}\hat{b}}$.

To conclude, resolution in the spatial domain is provided by comparing emission along the different collimated views. A synthetic diagnostic allows assessment of expected emission patterns from RE beams of constant n_{RE} and different r_{beam} and E_e (assuming zero pitch-angle). A radial profile can be formed by looking along the line of low $\theta_{\hat{k}\hat{b}}$, and experimental data finds different increasing spatial gradients with increasing E_γ. Angular profiles can be generated by comparing views of the same flux surface with different $\theta_{\hat{k}\hat{b}}$, pointing to future energy and pitch-angle resolved f_e inversions.

IV. RESOLVING THE ENERGY DOMAIN: RE DISTRIBUTION FUNCTIONS

This section will describe how the energy spectrum (f_γ) of incoming HXR pulses can be converted into 1-D RE energy distribution functions (f_e). The dependence

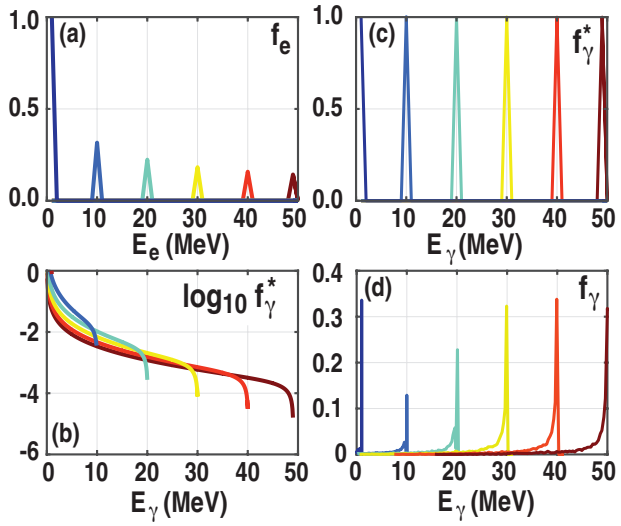

FIG. 9. Convolutions used in f_e inversion. (a) A mono-energetic f_e translates to (b) a spectrum of HXRs (f^*_γ) from bremsstrahlung. (c) A mono-energetic f^*_γ then undergoes (d) Compton scattering inside the scintillating crystal spreading f^*_γ into the final measured f_γ.

of the inverted f_e on experimental actuators will then be described alongside comparison to modeling.

A. Inversion Technique

The raw experimental measurement of the GRI system is a spectrum of HXR energies from individual HXR scintillation events. To go from this spectrum (f_γ) to the RE distribution function (f_e), two convolutions are needed - first the conversion from f_e in the plasma to the incident HXR distribution entering the detector volume. This intermediate distribution is termed f^*_γ. The second convolution takes f^*_γ to the final HXR distribution (termed f_γ) measured by scintillation light exiting each detector crystal.

The first convolution relies on computation of bremsstrahlung rate coefficients [43] together with sight-line geometric information. The same synthetic diagnostic tool used in Sec. III is again used to calculate the HXR energy spectrum (f_γ) from a series of mono-energetic E_e. Figure 9(b) shows the results of this convolution for a series of mono-energetic f_e spaced 10 MeV apart [Fig. 9(a)] for a central viewing sight-line. Experimental inversions typically use spectra from mono-energetic f_e spaced 1 MeV apart.

The second convolution relies on knowledge of the scintillating crystal geometry and material properties to calculate the expected Compton scattering within the crystal using Monte-carlo methods. This technique is used to compute the registered E_γ on the detector from a mono-energetic beam of incident HXRs [44]. The results of these calculations for the GRI BGO scintillating crystals are shown in Fig. 9(c)-(d) for an input mono-energetic f^*_γ.

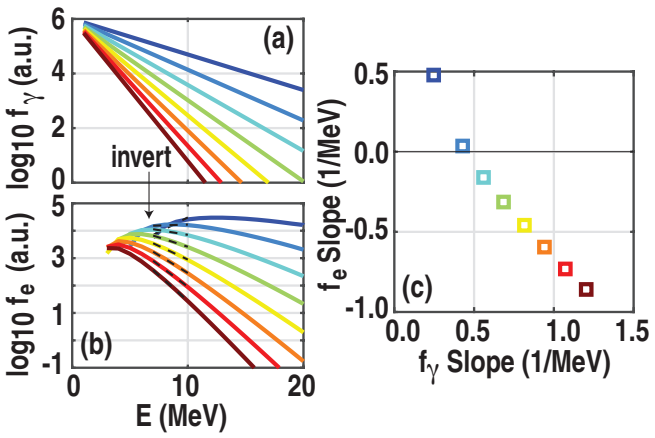

FIG. 10. Inversion results for (a) a family of f_γ with different slopes, which (b) map to either peaked, flat, or inverted f_e. (c) Summarizes the relationship between f_e and f_γ slope.

These two convolutions are performed together to compute the expected f_γ from mono-energetic f_e. The inversion process can then proceed using this information together with an onion-peel method, taking a key assumption: the maximum E_γ recorded is taken to be the maximum E_e in f_e. With this assumption, the number of REs at the maximum E_γ ($\equiv E_e$) is calculated to match the observed E_γ. The full f_γ expected from this E_e is then subtracted from the measured f_γ. This process then repeats working downwards from high to low energy, subtracting the expected f_γ from progressively lower E_e, until no residual f_γ remains. The number of REs needed at each E_e to account for the residual E_γ thus forms f_e. Since all operations are linear, the calculated f_γ from the inverted f_e always matches the original f_γ.

Uncertainty can also be propagated through this process. Underlying uncertainties are based on Poisson counting-statistics ($(\#\gamma)\pm\sqrt{(\#\gamma)}$), and these uncertainties are propagated in quadrature through the onion-peel process. In this way, the absolute f_e uncertainties are always larger as E_e decreases, but the fractional uncertainty can be significantly smaller if f_e increases with decreasing E_e. To minimize experimental uncertainty, long duration collection times (≈ 2 s) during stationary periods are used, as well as aggregating pulses collected from multiple spatial views. This increases the raw number of counts and thus reduces the fractional uncertainty.

Whether a given f_e is peaked, flat, or inverted depends on the local slope of f_γ. This is shown in Fig. 10, where the inversion results from a family of f_γ defined by a single slope are shown. For a steep slope in f_γ, f_e is inverted to be peaked, while for shallow f_γ, f_e is inverted to be non-monotonic. This demonstrates that in principle the GRI diagnostic can differentiate between each type of distribution, with f_γ slope playing a crucial role.

Some assumptions are necessary for the inversion process to be tractable. The first is spatial homogeneity: the same RE phase-space distribution function is assumed to

exist throughout the sight-line. As discussed in Sec. III, this is less important at high E_e since the emission tends to be localized to a smaller volume, but at low E_e this is no longer true. Secondly, finite pitch-angle effects are ignored in the inversions, though as discussed in Sec. III B further work should enable full 2-D inversions. Alternate inversion processes are also possible, either using weight-function techniques [45, 46] or tools such as DeGaSum [47, 48].

B. Distribution Function Parametric Dependencies

The inversion process described above is deployed to compare experimentally reconstructed f_e across changes in experimental actuators as well as to compare between modeling and experiment. As discussed in Sec. II B, changes in electron density (n_e) and toroidal field (B_T) map onto changes of E/E_C (Eq. 1) and $\hat{\tau}_{rad}$ (Eq. 2) to vary the collisional and synchrotron damping respectively. These non-dimensional parameters are expected from modeling to strongly influence the shape of f_e.

Results are summarized in Fig. 11. First, considering experimental f_e at different n_e [different E/E_C, Fig. 11(a)], non-monotonicity is observed in the lower energy part of the spectrum. As n_e is increased from 1.0×10^{19} m^{-3} to 1.5×10^{19} m^{-3}, large changes in f_e are measured well after t_{puff}. The spectrum is significantly shifted to lower energy and the location of the non-monotonic feature also shifts from ≈ 7 to 5 MeV. Considering modeling (discussed in Sec. II C) of the same experimental conditions [Fig. 11(b)], agreement is found in some areas. First, the predicted f_e contain non-monotonic features at consistent energies to the experimental f_e. Second, increasing n_e shifts f_e to lower energy in both modeling and experiment. The main discrepancy is that f_e is narrower in experiment than modeling, with f_e limited to lower energy. Possible reasons for this discrepancy will be discussed in Sec. VI.

The effect of synchrotron damping is studied by varying B_T to affect $\hat{\tau}_{rad}$, holding n_e and Z constant. Looking several seconds after t_{puff}, significant changes in both experimental and modeled f_e are found. Experimentally [Fig. 11(c)], opposite effects on f_e are observed at high and low E_e. The largest B_T cases are limited to the lowest maximum E_e, consistent with the maximum energy limit being set by synchrotron damping. An opposite effect is found at low E_e, where the largest B_T case contains the largest low E_e population. Since E/E_C is not varying, this is thought to be due to an advective process where at low B_T the particles at low E_e have simply energized to high E_e.

Comparing with modeling of the $\hat{\tau}_{rad}$ effect [Fig. 11(d)], the same qualitative picture is found but with significant quantitative differences. Note first the axis scale is significantly narrower for experimental results, again confirming the narrower nature of the experimental f_e. The opposite behavior at low and high E_e is reproduced, but the 'neutral point' is as 20 MeV in modeling vs. 6 MeV in experiment. Discussion of these differences will be left to the following section, as the discrepancies are not limited to the energy domain.

To conclude, resolution in the energy domain can be obtained through pulse height analysis to measure f_γ that in turn can be inverted to f_e with some assumptions. This enables comparison of experimental and modeled f_e when varying experimental actuators to vary synchrotron and collisional damping. Qualitative agreement is found on the role of these actuators, though quantitative differences are also identified. Measurements are also consistent with predictions of phase-space attractors that accumulate REs and form non-monotonic features in the RE energy distribution.

V. RESOLVING THE TIME DOMAIN: RE GROWTH AND DECAY

Slowly varying plasma parameters in the low-density scenario ensures sufficient temporal resolution is available for all diagnostics described in Sec. II A. A complete time-evolution for a well diagnosed discharge is shown in Fig. 12(a)-(e). This discharge included a rise in B_T and a relatively small density rise insufficient to bring the emission measured by the distant HXR detector into decay. Very different growth rates are observed across the different diagnostics as summarized in Fig. 12(g). HXR growth rates measured by the GRI system are plotted against the HXR energy (E_γ), while other diagnostics are shown as bands owing to their uncertain energy weighting. This indicates the consistency of the GRI growth rates with the energy weighting shown in Fig. 2: ECE growth rates are comparable to low E_γ GRI growth rates while high E_γ GRI growth rates are comparable to SE. While the energy weighting of the distant HXR is unknown, it is found to generally match the low E_γ GRI growth rates.

The isolated effects of collisional damping and synchrotron damping will now be considered in Secs. V A and V B. To compare modeled growth rates to the GRI system, a conversion from the time-dependent modeled RE distribution f_e to the HXR distribution f_γ is needed. This is achieved with the GRI synthetic diagnostic described in Sec. III, run for many time slices. The time-dependence of f_e thus maps onto f_γ time dependence, which is then fit to an exponential function at each E_γ.

A. Effect of Toroidal Field (Synchrotron Damping)

As toroidal field enters quadratically into $\hat{\tau}_{rad}$ (Eq. 2), this actuator has a strong effect on emission growth rates as shown in Fig. 13(a). While distant HXR and ECE growth rates increase with increasing B_T, the SE growth rate decreases. Qualitatively this can be understood as the low E_e RE population decaying more slowly as B_T

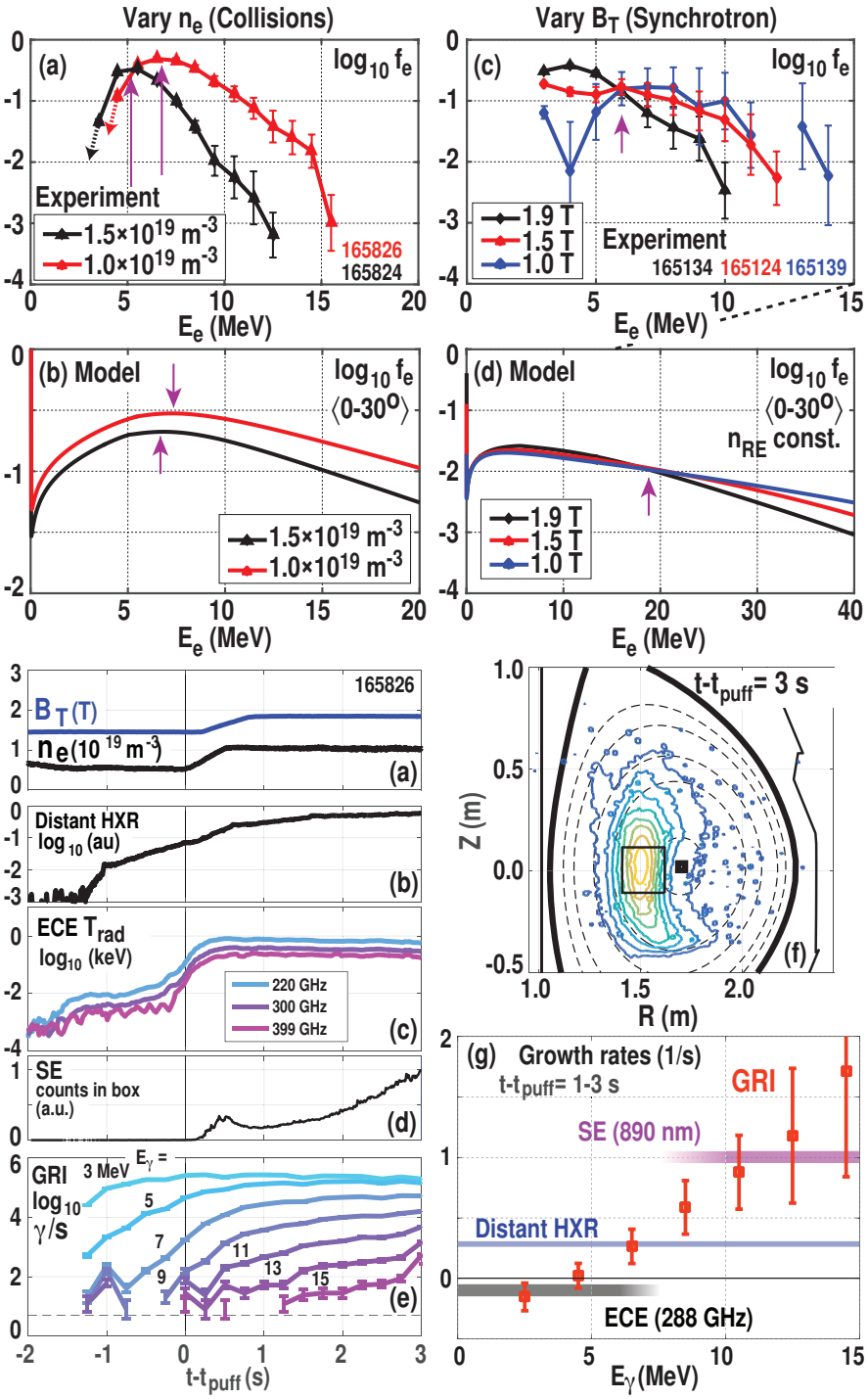

FIG. 11. (a,c) Experimental and (b,d) modeled f_e under the effect of (a,b) n_e and (c,d) B_T variations to identify f_e sensitivities to E/E_C and $\hat{\tau}_{rad}$.

FIG. 12. Time evolution of the discharge across several diagnostics. (a) Increases in B_T and n_e together after t_{puff} cause changes in diagnostic growth rates. (b) HXR grows slowly, while (c) ECE is essentially stationary, and (d) SE grows robustly with (f) a HFS-localized emission pattern. Note time-dependence of SE in (d) is obtained by integrated the number of counts in the central box shown in (f). (e) Different GRI growth rates are found at each E_γ, which summarizing in (g) indicates consistency with the other diagnostics.

increases while the highest E_e RE population grows more slowly as B_T increases. These measurements are consistent with E_γ-resolved HXR growth rate analysis from the GRI, shown in Fig. 13(b). At low E_γ, the HXR growth rate increases with increasing B_T while the high E_γ growth rate decreases. These f_γ growth rate changes also demonstrate how the differences in f_e with B_T shown in Fig. 11(c) arose over time. Initial f_e were strongly decaying with E_e but over time the low B_T case became the most numerous at high E_e and least numerous at low E_e.

Model predictions of the HXR growth rates, shown in Fig. 13(c), reveal the same qualitative trend. At low E_γ growth rates increase with B_T while the opposite occurs at high E_γ. In modeling the growth rates cross each other at ≈ 8 MeV, compared to 5 MeV in experiment. However, the large experimental growth rates shown in Fig. 13(b) with $E_\gamma > 8$ MeV are not recovered until much higher E_γ in modeling. Note also the different E_γ axis limits of Fig. 13(b)-(c). Thus the quantitative effect of varying synchrotron damping is found to be larger in

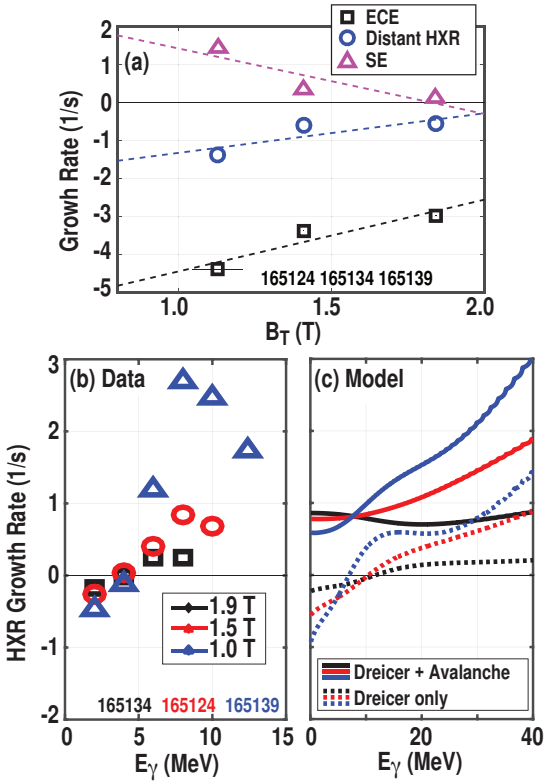

FIG. 13. Dependence of emission growth rates (from 1 to 3 s after $t_{\rm puff}$) on B_T at fixed n_e of 2.5 $\times 10^{19}$ m^{-3} (fixed $E/E_{\rm C}$). (a) Different dependencies are found for diagnostics sensistive to low and high E_e populations. (b,c) E_γ-resolved GRI emission growth comparing (b) experiment and (c) modeling.

experiment than modeling.

This discrepancy may be due to the omission of spatial effects in the present modeling, since SE is itself dominated by the HFS region of the plasma [see Fig. 12(f)] where B and thus the local $\hat{\tau}_{\rm rad}$ is higher. Recent work has also identified the important role of full-orbit spatial effects in enhancing the synchrotron force, with a several-fold increase in stopping power reported [28].

Focusing on the behavior at low energy ($E_\gamma < 5$ MeV), a stark qualitative discrepancy is found at all B_T. While the HXR emission is predicted to grow in modeling, it decays in experiment and thus indicates anomalous RE loss. Repeating simulations with the avalanche mechanism artificially turned off (dashed lines in Fig. 13(c)) causes the expected signal to decay, as in the experiment. This is only illustrative as in these conditions ($E/E_{\rm C} \approx 4$) avalanching should still occur. A sizeable effect, comparable to the avalanche mechanism, is thus missing from modeling. Possible causes for this will be further described in Sec. VI.

While discharges ramping B_T upwards exhibit fairly consistent growth rates in time (as in Fig. 12), ramping B_T downwards must be done over very long time scales due to hardware constraints. These discharges thus never reach a stationary condition, and complex temporal dependencies are observed, shown in Fig. 14. While the distant HXR emission and low energy GRI bins are characterized by a single decay rate, high energy GRI bins and SE images transition from an early growth phase shortly after $t_{\rm puff}$ to a decaying phase after $t - t_{\rm puff}$=2 s.

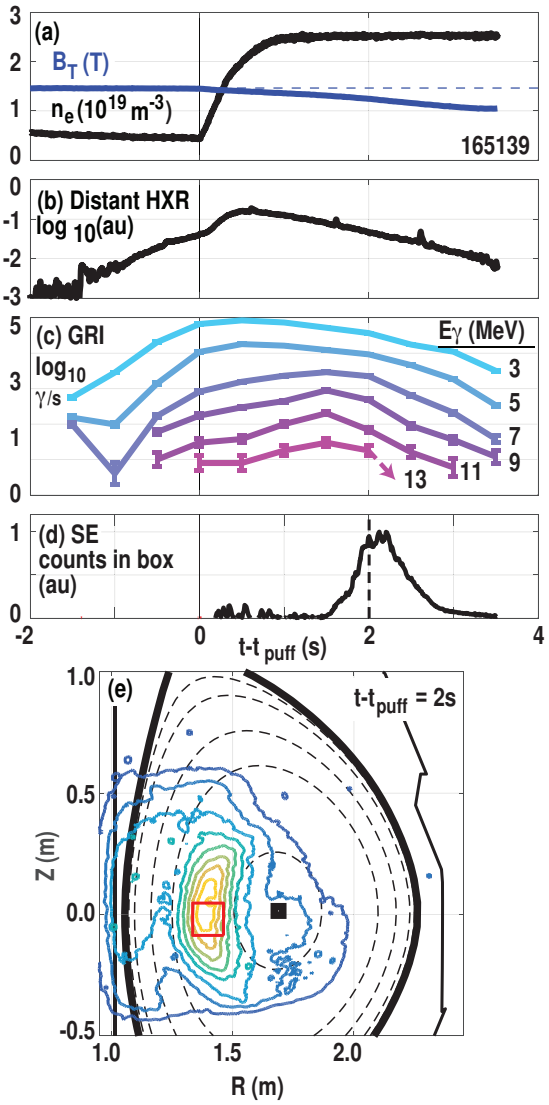

FIG. 14. Complex temporal dependencies for discharges where (a) B_T slowly decreases at fixed n_e. (b) Distant HXR detectors show consistent decay, while (c) high energy GRI and (d) SE show signal growth followed by signal decay. The late decay phase corresponds to (e) increased SE from the region near the center-post, suggesting RE loss.

This effect is interpreted as a two-part process. First f_e reaches higher peak energy due to the reduction of the synchrotron force. As the REs energize it appears they eventually become deconfined through either a drift orbit effect or some other loss mechanism. This is supported by SE images indicating a region of interaction with the center-post later in time, shown in Fig. 14(e).

To conclude, while the effect of synchrotron damping on RE growth is qualitatively as expected, the comparison shown in Fig. 13 indicates that: 1) the quantitative effect from changing B_T is larger than in modeling, and 2) a significant anomaly exists at low E_γ, where HXR

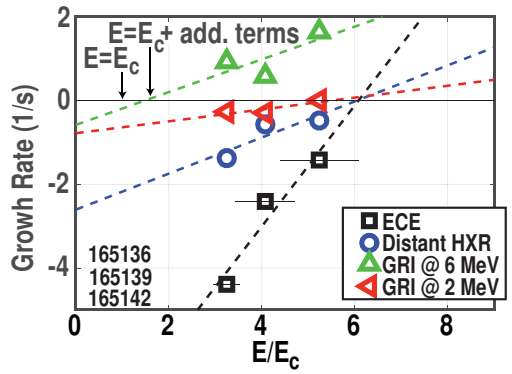

FIG. 15. Dependence of emission growth rates on E/E_C, indicating only high E_γ HXRs extrapolate to a E/E_C zero crossing that is more consistent with the theory in Ref. [9]. Discharges at low B_T are presented but findings are similar at other B_T values. $Z \approx 1$ for these discharges.

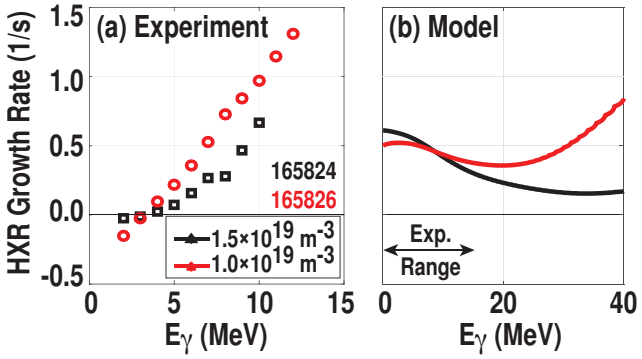

FIG. 16. (a) Experimental and (b) modeled HXR growth rates as a function of HXR energy (E_γ) for the cases shown in Fig. 11(a)-(b). $Z \approx 3-4$ for these discharges.

growth is predicted yet decay is observed.

B. Effect of Electron Density (Collisional Damping)

As the collisional damping rate is proportional to n_e, Eq. 1 shows E/E_C is inversely proportional to n_e. Consistent with previous examinations of the n_e effect on emission growth rates [18, 19], strong sensitivity to E/E_C is found together with a transition from HXR growth to decay at an anomalously large value of E/E_C. Figure 15 demonstrates this result extends to several diagnostics sensitive to low energy REs (ECE, distant HXR, and low energy GRI), but not GRI measurements at high energy. Low energy diagnostics show a transition from emission growth to decay at $E/E_C \approx 6$, which is far in excess of the theoretical expectation even after accounting for expected dissipation enhancement from synchrotron and pitch-angle scattering. These additional dissipation terms raise the expected transition from $E/E_C = 1$ to 1.6 in these conditions. In contrast, examining the emission trend from higher energy HXRs measured by the GRI, the extrapolated transition to HXR decay is at an E/E_C value much more consistent with the theory in Ref. [9] (that includes the additional synchrotron and pitch-angle scattering dissipation terms). This suggests the anomalous dissipation of REs is most pronounced at low energy.

Direct comparison of experimental and modeled HXR growth rates as a function of E_γ is shown in Fig. 16 for two different n_e levels. These discharges featured injection of nitrogen to raise Z to between 3-4, with n_e controlled by feedback. Note the lower n_e case is also described in Fig. 12. The increased Z increased bremsstrahlung emission and thus signal to noise, enabling more resolved energy-dependent growth rates to be extracted to high energy. Qualitative similarities and differences exist with modeling. Both modeled and experimental growth rates are between 0.5 to 1.5 1/s, both demonstrate increasing growth rate as E_γ increases, and both find reduced growth rates as n_e increases. However, the horizontal axis is compressed in the experiment, similar to findings shown in Fig. 13. Also consistent with Fig. 13, at low E_γ HXR growth is expected, yet decaying or flat HXR signals are observed. Interestingly, the very lowest E_γ growth rates display an opposite dependence to n_e as in Fig. 15, presumably due to the presence of high Z in the discharges of Fig. 16. These discrepancies will be further discussed in Sec. VI.

To conclude this final section, time domain resolution is obtained by tracking emission rates as a function of time. Simultaneous growth and decay of different emission bands is observed, and consistency is found between energy-resolved HXR growth rates and other emission bands thought to probe low (ECE) and high (SE) energy REs. Increasing synchrotron damping by raising B_T reduces the growth rate of the high E_γ emission, while increasing n_e decreases the growth rate at nearly all energies. Modeling qualitatively recovers these effects, though discrepancies are found as will be discussed in the next section.

VI. DISCUSSION AND CONCLUSION

In this work diagnostic resolution in the spatial, energy, and temporal domain has yielded novel measurements of RE dependencies to plasma parameters. Broadly speaking, this work has enabled unique opportunities for model validation, and as such improves confidence that model-based optimization of RE control and avoidance can be achieved. In this section observations are summarized highlighting areas of agreement and disagreement with modeling, followed by discussions of possible resolutions to the identified discrepancies, and finally this work concludes with a discussion of future directions for research.

A. Summary of Observations and Discrepancies with Modeling

Energy resolution finds qualitative agreement of distribution function changes with collisional and synchrotron

damping: increased collisional damping reduces the energy of f_e throughout, while increased synchrotron damping reduces the high-energy part of f_e. Many f_e are found to develop non-monotonic features as the discharge develops, and the energy of these features are consistently predicted by modeling. Consistently across all conditions, experimentally measured f_e appear 'narrower' than predicted, with f_e decreasing with energy faster in experiment. Time resolution reveals that considering the HXR growth rate as a function of energy yields consistent (and with improved resolution) growth rates to other diagnostics. Quantitative discrepancies with predicted growth rates are found for all energies, but the most severe qualitative discrepancy is found at low energy. Decay of low energy HXRs are observed, for E/E_C up to $\approx$5, while growth is predicted for $E/E_C > 1.6$. Consistently, spatial resolution identifies radial gradients of the RE population, with the lowest gradients (and thus presumably the largest transport) found at low energy. Possible resolutions to these discrepancies are now described.

B. Possible Resolutions to Discrepancies

Modeling utilized to describe this work takes into account the physical mechanisms thought to be important for the RE distribution function, such as Dreicer generation, avalanche multiplication, collisional damping, synchrotron damping, and pitch-angle scattering. However, potentially important aspects are still missing, the most important of which are proposed here to be spatial transport and the role of kinetic instability.

As described in Sec. III A, radial gradients are found in the RE population. These gradients could be related to a core source and radial diffusive flux term, by experimentally fitting a diffusion coefficient that matches the data (varying with energy). However, modeling at present is unable to predict the RE diffusion from first principles without knowing the magnitude and spectrum of the fluctuating magnetic field components. Thus it is difficult to quantify the role of spatial diffusion, though admittedly the fact that gradients are weakest at low energy is contrary to simple expectations for fluctuation-based RE transport. Future experiments may explore the role of spatial diffusion more carefully by varying the magnitude of the thermal confinement and also by exploring effects due to imposed non-axisymmetric magnetic perturbations.

A second possibility is kinetic instability of the RE beam itself. This would manifest itself as waves driven by the RE population through either the Cerenkov, normal Doppler, or anomalous Doppler resonances. A wide spectrum of waves can be driven by the RE population, and indeed the non-monotonic f_e found in these studies should have a strong drive for kinetic instability. Recent work has identified a strong drive for magneto-sonic waves at 10s of GHz from these f_e [49], and interestingly the resonances leading to the strongest RE diffusion are found at low E_e, where the largest discrepancy with modeling is found. Future dedicated work will thus focus on the potential role of kinetic instability to explain the discrepancies found in these studies. It should however be noted that the keV-level T_e Ohmic plasmas used for this study are rather collisionless and thus only weakly damp kinetic instabilities. In contrast, the much colder and collisional conditions (eV-level T_e) of the post-disruption ITER RE beam suggests it is should be significantly harder for kinetic instability to play a role in post-disruption RE dissipation [50].

C. Future Directions

Beyond the model improvements described in Sec. VI B, future experimental and analysis work is planned along several fronts. Firstly, measurements here focus on the low-density RE regime. At present, measurements in the post-disruptive RE regime on DIII-D [3] have been limited due to the much higher HXR fluxes saturating the GRI diagnostic. Increased shielding and improved electronics are planned to reduce the stray HXR flux and also increase the maximum count rate. Further, measurements here included only a subset of the available 'pixels' due to a limited number of detectors. Planned upgrades will double the number of active channels to fully exploit the spatial resolution of the GRI diagnostic. Considering inversions of f_γ to f_e, work is planned to include finite pitch-angle effects in the synthetic diagnostic used to generate the HXR spectra shown in Fig. 9. Utilizing multiple views of the same flux surface to gain pitch-angle resolution should allow a full energy and pitch-angle resolved inversion of the RE distribution function.

ACKNOWLEDGMENTS

DIII-D data shown in this paper can be obtained in digital format by following the links at `https://fusion.gat.com/global/D3D_DMP`. The authors thank J. Kulchar, D. Taussig, M. Austin, S. Haskey, B. Grierson, R. Groebner, and Y. Zhu for diagnostic support, as well as N. Commaux and A. Wingen for their assistance. This material is based upon work supported in part by the U.S. Department of Energy under Grants DE-FC02-04ER54698, DE-FG02-07ER54917, DE-AC05-00OR22725, DE-FC02-99ER54512, DE-SC0016268.

[1] T. C. Hender, J. C. Wesley, J. M. Bialek, A. Bondeson, A. H. Boozer, R. J. Buttery, A. M. Garofalo, T. P. Goodman, R. S. Granetz, Y. Gribov, O. Gruber, M. P. Gryaznevich, G. Giruzzi, S. Günter, N. Hayashi, P. Helander, C. C. Hegna, D. F. Howell, D. A. Humphreys, G. T. A. Huysmans, A. W. Hyatt, A. Isayama, S. C. Jardin, Y. Kawano, A. G. Kellman, C. E. Kessel, H. R. Koslowski, R. J. LaHaye, E. Lazzaro, Y. Liu, V. Lukash, J. Manickam, S. Medvedev, V. Mertens, S. V. Mirnov, Y. Nakamura, G. A. Navratil, M. Okabayashi, T. Ozeki, R. Paccagnella, G. Pautasso, F. Porcelli, V. D. Pustovitov, V. Riccardo, M. Sato, O. Sauter, M. J. Schaffer, M. Shimada, P. Sonato, E. J. Strait, M. Sugihara, M. Takechi, A. D. Turnbull, E. Westerhof, D. G. Whyte, R. Yoshino, H. Zohm, D. Group, the Itpa Mhd, and Magnet, Nuclear Fusion **47**, S128 (2007).

[2] M. Lehnen, K. Aleynikova, P. B. Aleynikov, D. J. Campbell, P. Drewelow, N. W. Eidietis, Y. Gasparyan, R. S. Granetz, Y. Gribov, N. Hartmann, E. M. Hollmann, V. A. Izzo, S. Jachmich, S.-H. Kim, M. Kočan, H. R. Koslowski, D. Kovalenko, U. Kruezi, A. Loarte, S. Maruyama, G. F. Matthews, P. B. Parks, G. Pautasso, R. A. Pitts, C. Reux, V. Riccardo, R. Roccella, J. A. Snipes, A. J. Thornton, and P. C. de Vries, Journal of Nuclear Materials **463**, 39 (2015).

[3] E. M. Hollmann, P. B. Aleynikov, T. Fülöp, D. A. Humphreys, V. A. Izzo, M. Lehnen, V. E. Lukash, G. Papp, G. Pautasso, F. Saint-Laurent, and J. A. Snipes, Physics of Plasmas **22**, 021802 (2015).

[4] A. H. Boozer, Physics of Plasmas **22** (2015), 10.1063/1.4913582.

[5] J. W. Connor and R. J. Hastie, Nuclear Fusion **15**, 415 (1975).

[6] M. N. Rosenbluth and S. V. Putvinski, Nuclear Fusion **37**, 1355 (1997).

[7] J. R. Martin-Solis, J. D. Alvarez, R. Sanchez, and B. Esposito, Physics of Plasmas **5**, 2370 (1998).

[8] F. Andersson, P. Helander, and L.-G. Eriksson, Physics of Plasmas **8**, 5221 (2001).

[9] P. B. Aleynikov and B. N. Breizman, Physical Review Letters **114**, 155001 (2015).

[10] P. B. Aleynikov, K. Aleynikova, B. N. Breizman, G. T. A. Huijsmans, S. V. Konovalov, S. V. Putvinski, and V. Zhogolev, in *Proc. of 25th IAEA Fusion Energy Conf. (St. Petersburg, Russia)* (2014) pp. TH/P3–38.

[11] E. Hirvijoki, I. Pusztai, J. Decker, O. Embréus, A. Stahl, and T. Fülöp, Journal of Plasma Physics **81**, 475810502 (2015), arXiv:1502.03333.

[12] A. Stahl, E. Hirvijoki, J. Decker, O. Embréus, and T. Fülöp, Phys. Rev. Lett. **114**, 115002 (2015).

[13] C. Liu, D. P. Brennan, A. H. Boozer, and A. Bhattacharjee, Physics of Plasmas **23**, 1 (2016), arXiv:1509.04402.

[14] J. Decker, E. Hirvijoki, O. Embréus, Y. Peysson, A. Stahl, I. Pusztai, and T. Fülöp, Plasma Physics and Controlled Fusion **58**, 025016 (2016).

[15] C. Liu, D. P. Brennan, A. H. Boozer, and A. Bhattacharjee, Plasma Physics and Controlled Fusion **59**, 024003 (2017).

[16] Z. Guo, C. J. Mcdevitt, and X. Tang, Plasma Physics and Controlled Fusion **59**, 044003 (2017).

[17] J. R. Martin-Solis, R. Sánchez, and B. Esposito, Physical Review Letters **105**, 185002 (2010).

[18] C. Paz-Soldan, N. W. Eidietis, R. S. Granetz, E. M. Hollmann, R. A. Moyer, N. A. Crocker, A. Wingen, and Y. Zhu, Physics of Plasmas **21**, 022514 (2014).

[19] R. S. Granetz, B. Esposito, J. H. Kim, R. Koslowski, M. Lehnen, J. R. Martin-Solis, C. Paz-Soldan, T. Rhee, J. C. Wesley, L. Zeng, and I. M. Group, Physics of Plasmas **21**, 072506 (2014).

[20] E. M. Hollmann, P. B. Parks, D. A. Humphreys, N. H. Brooks, N. Commaux, N. W. Eidietis, T. E. Evans, R. Isler, A. N. James, T. C. Jernigan, J. Munoz, E. J. Strait, C. Tsui, J. C. Wesley, and J. H. Yu, Nuclear Fusion **51**, 103026 (2011).

[21] E. M. Hollmann, P. B. Parks, N. Commaux, N. W. Eidietis, R. A. Moyer, D. Shiraki, M. E. Austin, C. J. Lasnier, C. Paz-Soldan, and D. L. Rudakov, Physics of Plasmas **22**, 056108 (2015).

[22] C. Paz-Soldan, C. M. Cooper, P. B. Aleynikov, D. C. Pace, N. W. Eidietis, D. P. Brennan, R. S. Granetz, E. M. Hollmann, C. Liu, A. Lvovskiy, R. A. Moyer, and D. Shiraki, Physical Review Letters **118**, 255002 (2017).

[23] D. C. Pace, C. M. Cooper, D. Taussig, N. W. Eidietis, E. M. Hollmann, V. Riso, and M. A. V. Zeeland, Review of Scientific Instruments **87**, 043507 (2016).

[24] C. M. Cooper, D. C. Pace, C. Paz-Soldan, N. Commaux, N. W. Eidietis, E. M. Hollmann, and D. Shiraki, Review of Scientific Instruments **87**, 11E602 (2016).

[25] R. Jaspers, N. Cardozo, and K. H. Finken, Physical Review Letters **72**, 4093 (1994).

[26] J. H. Yu, E. M. Hollmann, N. Commaux, N. W. Eidietis, D. A. Humphreys, A. N. James, T. C. Jernigan, and R. A. Moyer, Physics of Plasmas **20**, 042113 (2013).

[27] R. J. Zhou, I. M. Pankratov, L. Q. Hu, M. Xu, and J. H. Yang, Physics of Plasmas **21**, 063302 (2014).

[28] L. Carbajal, D. Del-Castillo-Negrete, D. Spong, S. Seal, and L. R. Baylor, Physics of Plasmas **24**, 042512 (2017).

[29] M. Hoppe, O. Embréus, R. A. Tinguely, R. S. Granetz, A. Stahl, and T. Fülöp, (2017), arXiv:1709.00674.

[30] H. Dreicer, Phys. Rev. **115**, 238 (1959).

[31] C. Paz-Soldan, R. J. La Haye, D. Shiraki, R. J. Buttery, N. W. Eidietis, E. M. Hollmann, R. A. Moyer, J. E. Boom, and I. T. Chapman, Nuclear Fusion **56**, 056010 (2016).

[32] L.-G. Eriksson and P. Helander, Computer Physics Communications **154**, 175 (2003).

[33] P. Helander, *Collisional Transport in Magnetized Plasmas* (Cambridge University Press, 2002).

[34] G. Papp, M. Drevlak, T. Fülöp, and P. Helander, Nuclear Fusion **51**, 43004 (2011).

[35] P. B. Parks, M. N. Rosenbluth, and S. Putvinski, Physics of Plasmas **6**, 2523 (1999).
[36] P. B. Aleynikov and B. N. Breizman, Nuclear Fusion **57**, 046009 (2017).
[37] J. R. Martin-Solis, A. Loarte, and M. Lehnen, Nuclear Fusion **57**, 066025 (2017).
[38] V. Zhogolev and S. V. Konovalov, VANT series Nuclear Fusion **4** (2014).
[39] L. Hesslow, O. Embréus, A. Stahl, T. C. Dubois, G. Papp, S. L. Newton, and T. Fülöp, Physical Review Letters **118**, 1 (2017), arXiv:1705.08638.
[40] E. M. Hollmann, N. Commaux, N. W. Eidietis, C. J. Lasnier, D. L. Rudakov, D. Shiraki, C. Cooper, J. R. Martin-Solis, P. B. Parks, and C. Paz-Soldan, Physics of Plasmas **24**, 062505 (2017).
[41] C. Reux, V. Plyusnin, B. Alper, D. Alves, B. Bazylev, and E. Belonohy, Nuclear Fusion **55**, 093013 (2015).
[42] P. Helander, L.-G. Eriksson, and F. Andersson, Physics of Plasmas **7**, 4106 (2000).
[43] H. W. Koch and J. W. Motz, Review of Modern Physics **31**, 920 (1959).
[44] Y. Peysson and F. Imbeaux, Review of Scientific Instruments **70**, 3987 (1999).
[45] M. Salewski, M. Nocente, G. Gorini, A. Jacobsen, V. Kiptily, S. Korsholm, F. Leipold, J. Madsen, D. Moseev, S. Nielsen, J. Rasmussen, M. Stejner, and M. Tardocchi, Nuclear Fusion **56**, 046009 (2016).
[46] L. Stagner and W. W. Heidbrink, Physics of Plasmas **24** (2017), 10.1063/1.4990391.
[47] A. E. Shevelev, E. M. Khilkevitch, V. G. Kiptily, I. N. Chugunov, D. B. Gin, D. N. Doinikov, V. O. Naidenov, A. E. Litvinov, and I. A. Polunovskii, Nuclear Fusion **53**, 123004 (2013).
[48] A. E. Shevelev, E. M. Khilkevitch, S. I. Lashkul, V. V. Rozhdestvensky, and A. B. Altukhov, Nuclear Instruments and Methods in Physics Research A **830**, 102 (2016).
[49] C. Liu, E. Hirvijoki, G.-y. Fu, D. P. Brennan, A. Bhattacharjee, and C. Paz-Soldan, ArXiv e-prints (2018).
[50] P. B. Aleynikov and B. N. Breizman, Nuclear Fusion **55**, 043014 (2015).